Nucleation burst in additively manufactured Inconel 718: 3D characterization of ISRO-induced equiaxed microstructure

I. Cazic, Julien Zollinger, M. Engstler, J. Ghanbaja, T. Schenk, M. El Kandaoui, B. Appolaire

To cite this version:

I. Cazic, Julien Zollinger, M. Engstler, J. Ghanbaja, T. Schenk, et al.. Nucleation burst in additively manufactured Inconel 718: 3D characterization of ISRO-induced equiaxed microstructure. Additive Manufacturing, 2023, 66, pp.103458. 10.1016/j.addma.2023.103458 . hal-04213243

HAL Id: hal-04213243

https://hal.univ-lorraine.fr/hal-04213243v1

Submitted on 21 Sep 2023

Nucleation burst in additively manufactured Inconel 718: 3D characterization of ISRO-induced equiaxed microstructure

I. Cazic[a,b,c,**], J. Zollinger[a,b,*], M. Engstler[d], J. Ghanbaja[a], T. Schenk[a,b], M. El Kandaoui[c], B. Appolaire[a,b]

[a] *Université de Lorraine, Institut Jean Lamour, Campus ARTEM, Allée André Guinier, F-54011 Nancy, France*
[b] *Labex Damas, Université de Lorraine, Nancy, France*
[c] *Institut de Soudure, 4 bd Henri Becquerel, Espace Cormontaigne, 57970 Yutz, France*
[d] *Universität des Saarlandes, Department of Materials Science and Materials Engineering, Saarbrücken Campus, Germany*

Abstract

The origin of isosahedral short range order (ISRO)-mediated nucleation in additively manufactured Inconel 718 is investigated in this work. 3D EBSD-EDS characterisation of the equiaxed grain zone revealed a 5-fold symmetry axis emerging from the surface of a TiC particle. Using high resolution electron microscopy, the Nb_2Ni and Ni_6Nb_7 phases have been identified around a TiC particle for the first time in this alloy. Such phases are associated with local Nb enrichment around the TiC particles. The Nb-rich liquid and the solidification conditions of the additive manufacturing process induce the formation of phases containing a high concentration of icosahedral clusters and are thought to be the origin of ISRO-mediated nucleation in this alloy.

Keywords: Additive Manufacturing, Ni alloy, Solidification, Grain refinement, ISRO

---

1. Introduction

Additive manufacturing has emerged as an opportunity for the affordable production of near-net-shape components [1]. Coaxial wire feed laser metal deposition (LMD-W) has attracted increasing interest in recent years due to its low defect formation and clean processing environment [2, 3]. The low cost of the feedstock also gives this technology a great advantage for application in the aerospace industry compared to other processes [4] and is suitable for repairing damaged components [5]. Among the materials used in the aerospace industry, Inconel 718 is one of the most successful advanced alloys, which has attracted a large number of studies over the years [6, 7]. Recently, the production of Inconel 718 using LMD-W showed promising results as large zones of fine equiaxed grains were found at the bottom of the melt pools in the remelting regions of each layer [8–10]. As previously reported by the authors [9], the equiaxed grains form from an ISRO (Icosahedral Short-Range Order) mediated nucleation mechanism, which induces a significant reduction in grain size and an increase in grains with a twinning orientation relationship. This mechanism was first demonstrated by Kurtuldu *et al.* in Al-based and Au-based alloys [11, 12]. They have shown

---

[*] Corresponding author.
Email address: `julien.zollinger@univ-lorraine.fr`
[**] Present address: ACCESS e.V., Intzestr. 5, 52072 Aachen, Germany. `i.cazic@access-technology.de`

Preprint submitted to Published in Additive Manufacturing, `https://doi.org/10.1016/j.addma.2023.103458` *March 21, 2023*

that the incorporation of small amounts of Cr into aluminium alloys or Ir into gold alloys significantly reduces grain size, with a disproportionate number of twinned grain boundaries. In addition, they have found that certain groups of adjacent grains exhibit a multiple twin relationship with a common $\langle 110 \rangle$ direction. This relationship can be observed in up to 5 adjacent grains and is consistent with the symmetry of a decahedron. Furthermore, up to 9 neighbouring grains can exhibit twinning symmetry, which is consistent with the symmetry of an icosahedron.

In nickel-based alloys, and in addition to the work presented by the authors [9], the same mechanism has been demonstrated in commercially pure Ni processed by laser powder bed fusion (LPB-F) [13], opening up new prospects for controlling grain growth morphology in additive manufacturing of Ni-based alloys. However, what causes ISRO-mediated nucleation in Ni-based alloys is still unclear, as no chemical addition has been reported in any study identifying this mechanism, and a large number of processes have induced fine equiaxed grains for a wide range of input linear energy [9]. Currently, local ISRO is attributed to metastable short-range configurations in the liquid due to rapid melting and cooling rates during AM processing [9, 13]. This hypothesis is likely to be correct, as numerous studies have focused on controlling the grain morphology resulting from solidification by ultimately adjusting the processing parameters to achieve much larger equiaxed grain sizes [14–16]. Furthermore, during solidification, microsegregation in the interdendritic regions leads to the formation of the eutectic between the Laves phase hexagonal C14 $(Ni, Cr, Fe)_2(Nb, Mo, Ti)$ (space group $P6_3/mmc$, a = $0.491\,\mathrm{nm}$ and c = $0.781\,\mathrm{nm}$ [17]) and the γ fcc matrix (space group Fm-3m, a = $0.345\,\mathrm{nm}$ [18]) commonly observed from casting to AM for Inconel 718 [19, 20]. The Laves phase is detrimental to mechanical properties and is usually dissolved by post heat treatment during the homogenisation step [21, 22]. The rapid melting and solidification conditions in AM can induce strong out-of-equilibrium solidification conditions that could induce ISRO through undercooling effects [23] and further promote not only Laves phase but also other metastable phase formations that could act as nucleating agents and induce twinning grain boundaries in the fcc phase [24].

In order to determine the causes of ISRO-mediated nucleation in Inconel 718 processed with LMD-W, this study has undertaken a detailed characterisation of the equiaxed zone using coupled 3D EDS-EBSD analysis and high resolution electron microscopy. It is shown that titanium carbide particles play a key role in this mechanism and also promote the nucleation of numerous previously unreported phases in Inconel 718.

2. Experimental procedure

2.1. Materials and processing

Samples of $150 \times 27 \times 10\,\mathrm{mm}^3$ using commercial Inconel 718 welding wire were processed using a Precitec CoaxPrinter laser head. The $1.2\,\mathrm{mm}$ diameter wire was purchased from SelectArc Group. The chemical composition of the wire used in this study, provided by the supplier, is shown in Table 1. The laser source is an IPG $10\,\mathrm{kW}$ Yb^{3+}–doped fibre solid-state laser with an operating wavelength of $1070\,\mathrm{nm}$. The working distance is $105\,\mathrm{mm}$ and the radius of the laser ring is $2.5\,\mathrm{mm}$. The stick-out (distance between the tip of the wire nozzle and the working surface) was set to $9\,\mathrm{mm}$. The gas flow nozzles were held at a distance of $8\,\mathrm{mm}$ from the melt pool. An argon flow rate of $15\,\mathrm{L/min}$ was set to limit oxidation. The samples were deposited along a continuous bidirectional scanning strategy using an ABB IRB 6640-185 robot. The bidirectional scanning strategy consists of alternating the building direction between each layer along the y-axis as schematically shown in Figure 1(a). A laser power of $2000\,\mathrm{W}$, a scanning speed of $1.2\,\mathrm{m/min}$ and a wire feed rate of $2\,\mathrm{m/min}$ were used to process the samples. A macrograph of the as-deposited material is shown in Figure 11(b) in the $x-z$ plane. The material deposited with these parameters is dense and free of macroscopic defects. The dark areas visible in the figure correspond to the equiaxed grain regions which will be examined in detail below. Chemical analysis by energy dispersive spectrometry (EDS) in the SEM did not reveal any significant change in the composition of the wire and the deposited material compared to the values given in Table 1, given the precision of the technique ($\pm 0.5\,\%$).

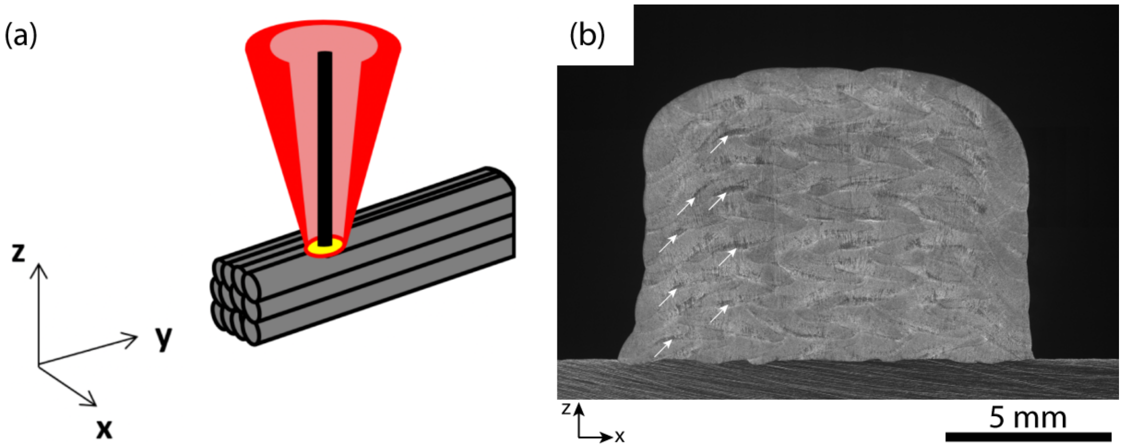

Figure 1: (a) Scanning strategy used to process the samples for microstructural characterization - y laser scan axis, z build axis. (b) Optical macrograph of the sample examined in the $x-z$ plane. The dark areas, some of which are indicated by white arrows, correspond to equiaxed fine grain areas.

Table 1: Chemical composition of the Inconel 718 wire used in this study.

Element	Ni	Cr	Fe	Nb	Mo	Ti	Al	Co	C	Mn	Si	Cu	Ta
mass. %	bal.	18.40	18.80	5.13	3.06	0.93	0.66	0.30	0.05	0.24	0.08	0.05	0.01

2.2. *Coupled 3D EDS-EBSD characterization*

Electron back-scattered diffraction (EBSD) and energy dispersive X-ray spectroscopy (EDS) were performed using a Thermo Fisher Helios Xe-PFIB focused ion beam scanning electron microscope equipped with an EDAX Velocity EBSD camera and an EDAX Octane EDS system. A step size of $1\,\mu\mathrm{m}$ was used for the large scale EBSD maps. To obtain 3D data, serial sections of $100\,\mathrm{nm}$ were taken in a volume of $60 \times 60 \times 60\,\mu\mathrm{m}^3$ in the equiaxed grain region. For each 2 slices, an EDS and EBSD 2D mapping with a resolution of 300×300 pixels was performed at $20\,\mathrm{kV}$, for a total of 300 EDS and EBSD images. From these images the 3D volume can be reconstructed with the EBSD data using the DREAM 3D software and visualized using the Avizo software. The voxel size is $200\times200\times200\,\mathrm{nm}^3$ (EBSD map step size of $200\,\mathrm{nm}$ and $200\,\mathrm{nm}$ between slices). Secondary electronic (SE) and back-scattered electronic (BSE) imaging to characterize the TiC particles was performed using a Zeiss Gemini SEM500 equipped with an InLens detector. EBSD analysis in 2D was performed using the Orix Python library [25] and HKL Channel 5 software. The $\Sigma3$ twinning boundary orientation relationship analysis was performed by identifying the grains with a rotation of $60°$ around a common $\langle 111\rangle$ axis, within an accuracy of $7.5°$ to account for the subgrain misorientations induced by the $7.35°$ aperture default angle associated with the decahedral configuration of 5 fcc tetrahedra [9].

2.3. TEM characterizations

Transmission electron microscopy (TEM) characterization was performed using a Jeol ARM 200F Cold FEG TEM/STEM operating at $200\,\mathrm{kV}$ and equipped with a spherical aberration (Cs) probe and image correctors (point resolution $0.19\,\mathrm{nm}$ in TEM mode and $0.078\,\mathrm{nm}$ in STEM mode). The microscope is equipped with both an EDS detector and an electron energy loss spectrometer (EELS). Thin foils for TEM were extracted in equiaxed grain regions and polished using a Helios Nanolab 600i electronic microscope with FIB technique. In the equiaxed region when using TEM, automated crystal orientation maps (ACOM) were performed using the ASTAR hardware and software [26]. Each diffraction pattern is acquired to assign a phase and orientation by comparing the diffraction spots with the simulated patterns of the different candidate phases [27].

2.4. Thermodynamics calculations

Thermodynamic calculations for the phase stability diagram were performed using the ThermoCalc software [28] (version 2021b) with the TTNI8 database. For these calculations, only the phases observed experimentally in this work were considered and the composition provided by the wire supplier was used. The calculations were carried out at temperatures relevant to the solidification of Inconel 718, i.e. between 1200 and $1400\,°\mathrm{C}$. Depending on the niobium content and within this temperature range, the purpose of the calculations was not to determine the most stable phases, but to determine if there was a driving force for the observed solid phases from the liquid phase to allow their nucleation.

3. Results

Figure 2(a) shows an EBSD map in the $y-z$ plane (where y is the laser scanning direction), complementary to the previously published data [9]. The figure shows the location of the boundary between two adjacent layers and the location of the equiaxed region within a layer that is closed to the melt pool boundary with the previous layer. The figure also shows where the TEM samples were taken (see section 3.2). For each region, *i.e.* columnar and equiaxed respectively, the misorientation angle distribution has been plotted including all grains in the map in Figure 2(b) and (c). The Mackenzie distribution for an isotropic grain distribution is given by the red dashed curve [29]. In the columnar region, the distribution is slightly shifted towards low angles due to growth parallel to the heat extraction. In the equiaxed region the distribution closely follows the Mackenzie distribution, but a large excess of misorientation angles can be seen at $60°$, indicating an anomalously high number of twins throughout the equiaxed region.

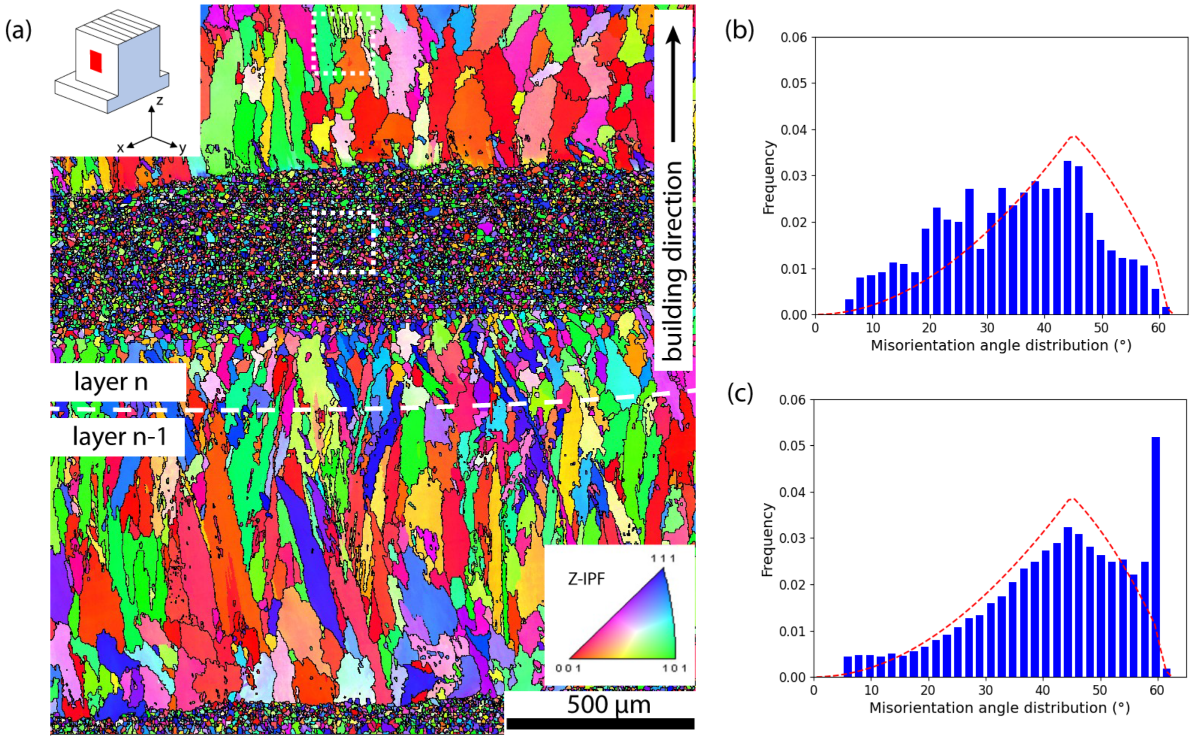

Figure 2: (a) EBSD map with IPF-z colouring of the sample in the $y - z$ plane. The boundary between the two adjacent layers is indicated by the white dashed line, while the dashed squares indicate the approximate location of the TEM samples. Distribution of misorientation angles for the (b) columnar and (c) equiaxed microstructures. The red dashed lines correspond to the Mackenzie distribution for an isotropic grain distribution [29].

3.1. 3D analysis of the equiaxed grain zone

The 3D $60 \times 60 \times 60\,\mu\mathrm{m}^3$ volume reconstructed from the EBSD IPF-z (building direction) data is shown in Figure 3. The analyzed volume contains 559 grains with an average grain size of $4.12 \pm 4.07\,\mu\mathrm{m}$, including edge grains. The equiaxed grains have no visible texture, as shown by the IPF coloring and both the (100) and (110) texture density plots.

In this volume, the grains with a $\Sigma 3$ twinning orientation relationship, i.e. grains sharing a common (111) plane, can be analyzed. Figure 4(a) shows the twinned grain boundaries in the volume corresponding to Figure 3. The fraction of twinned grain boundaries is $12.2\,\%$, which is much larger than the $0.13\,\%$ expected from an ensemble of randomly oriented equiaxed grains [29]. This figure is very close to the value of $12.8\,\%$ obtained from the 2D analyses which showed the presence of ISRO mediated nucleation in these alloys [9]. The difference between this

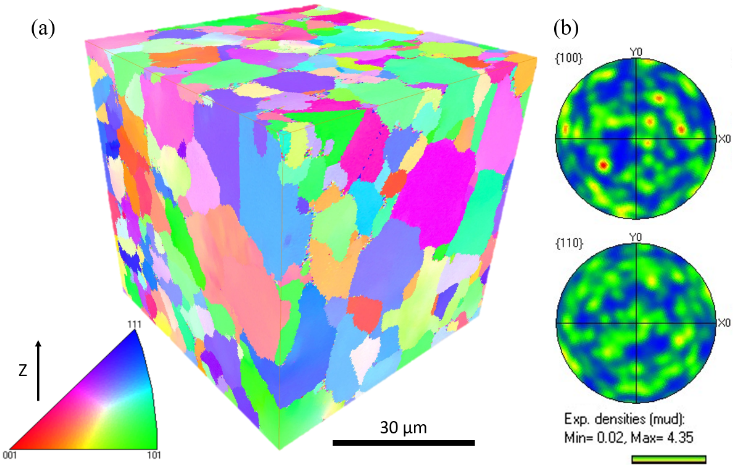

Figure 3: (a) 3D EBSD reconstruction of the analyzed volume of equiaxed grains with IPF-z coloring (b) texture density (100) and (110) pole figures.

value and the value observed in Figure 2(c) is due to the larger step size of the EBSD map used in Figure 2, which did not provide data for small grains, leading to an underestimation of the twin fraction. EDS analyses were conducted simultaneously with the EBSD measurements. These analyses highlighted the microsegregations that formed during the solidification of the alloy, but are outside the scope of this study. More relevant to the study of nucleation, the EDS measurements revealed numerous titanium carbide particles as shown in Figure 4(b). Two TiC particles populations are observed: (i) large particles in the range of 5 to $25\,\mu\mathrm{m}$, which were probably present before solidification began, and (ii) submicron particles, which probably nucleated during solidification due to microsegregation. The measured volume fraction of TiC is $1\,\%$.

From Figure 4(a), several sets of grains showing multiple twin orientation relationships have been identified. One of these is shown in Figure 5(a), where five grains, labeled 1 through 5, share a common $[110]$ axis (perpendicular to the figure). This is compatible with the 5-fold symmetry axis of an icosahedron, which is the signature of the ISRO-mediated nucleation mechanism. Looking at this set of grains from a different perspective and coupling the EBSD and EDS data gives a more surprising result, shown in Figure 5(b). In this figure, the common $[110]$ axis is now upright and appears to originate from a TiC particle. The presence of an aluminum oxide in the center of the carbide indicates that the TiC particle probably nucleated heterogeneously from the melt on the oxide particle. Titanium carbide has an fcc structure (NaCl structure type, space group Fm-3m, Pearson symbol cF8 [30]) with a lattice parameter of $0.435\,\mathrm{nm}$. The fcc Ni matrix has a lattice parameter of $0.359\,\mathrm{nm}$ in Inconel 718, which is lower than the TiC; however, a hetero-epitaxy relationship should be expected if the TiC would act as a substrate for heterogeneous nucleation.

To investigate the possible orientation relationship between the TiC and the five fcc-Ni grains presented above, a 2D slice containing them has been extracted and is shown in Figure 6(a) with IPF-z coloring. From this figure, the corresponding $\langle 110\rangle$ pole figure is shown in Figure 6(b). The common $[110]$ direction to the five grains is highlighted

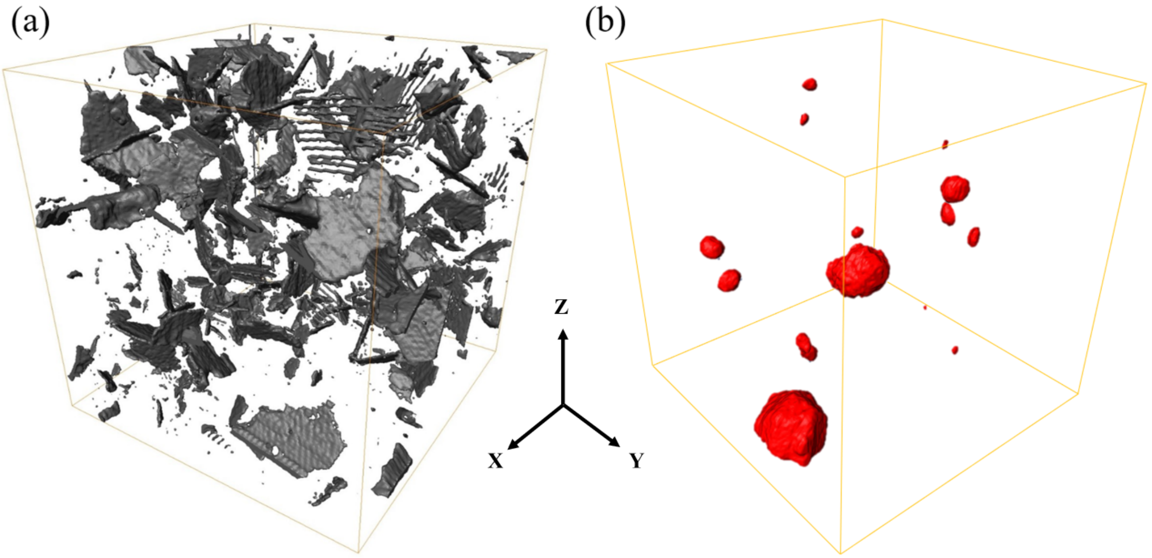

Figure 4: 3D reconstruction in the volume of (a) twin grain boundaries in dark gray (b) TiC particles identified by EDS.

by a red pentagon, and the red arcs indicate the trace of the common $\{111\}$ planes between each pair of grains. Each common $\{111\}$ plane between pairs of grains, i.e. 1-2, 2-3, 3-4 and 4-5, shows a rotation of $70.5°$ with respect to the previous one. As shown in a previous paper [9], this confirms the presence of a 5-fold symmetry axis. The common $\{111\}$ plane of grains 1 and 5 is rotated by 7-8° about the $[110]$ direction common to the five grains, which was defined by Kurtuldu *et al.* as a near-twin grain boundary. [11]. This set of 5 grains is compatible with the symmetry of a decahedron with grains 1 and 5, accommodating the aperture default angle of $7.5°$ [31]. No other fcc Ni grains were found with directions compatible with icosahedral symmetry. In Figure 6(b), the $\langle 110 \rangle$ directions of the TiC are shown with the purple star markers. None of these directions share a common pole with grains 1 to 5. It should be noted that the TiC particle has no orientation relationships with the fcc-Ni grains surrounding it.

The ISRO-mediated nucleation mechanism is based on the idea of nucleation on the facets of an icosahedral template. Based on this assumption, up to ten grains with orientation relationships compatible with icosahedral symmetry could be found. In the analyzed 3D volume only one 5-fold axis was found. This is probably due to the high thermal gradient induced by the process and the fact that the 5-fold axis is parallel to the building direction. It is very likely that other grains have an unfavorable growth direction compared to the thermal gradient. This latter observation, together with the fact that there is no relationship between the TiC particle and the surrounding grain, while the 5-fold symmetry axis seems to emerge from the particle, suggests that the mechanism governing nucleation here may be different from that proposed by Kurtuldu *et al.* [11, 12].

Figure 7(a) shows a SEM-SE image of a TiC particle in the equiaxed grain zone observed with the InLens detector at $1\,\mathrm{kV}$ accelerating voltage. These conditions allow the collection of a signal giving images with a contrast similar to that of back-scattered electrons (chemical and orientation contrast), but with excellent lateral and depth resolution

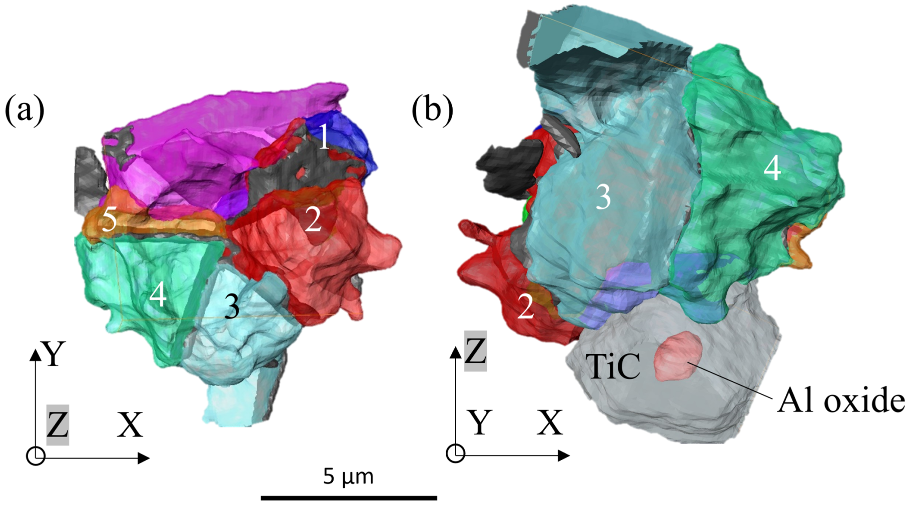

Figure 5: 3D view of (a) grains 1-2-3-4-5 sharing a multi-twinning OR with their corresponding IPF-z colors and twin grain boundaries in dark gray. An external grain in pink fills the void between grains 1-5 and has no relationship to the other grains. (b) 3D visualization of grains 1-2-3-4-5 and twin grain boundaries associated with the TiC particle (combining EBSD-EDS techniques). An Al oxide is identified in the center of the TiC particle.

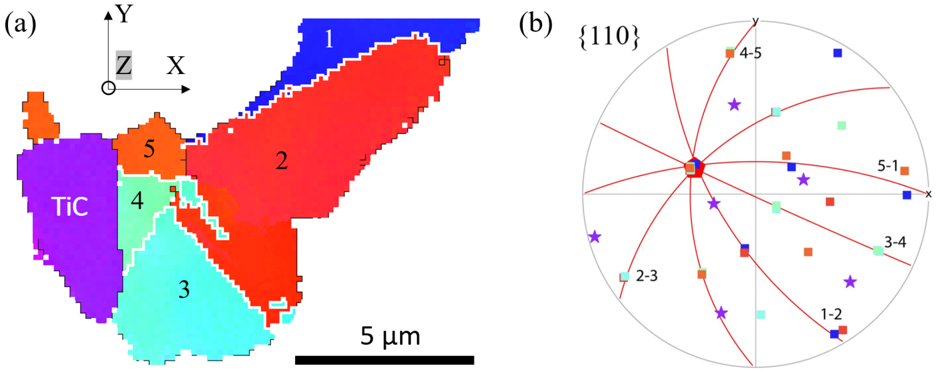

Figure 6: (a) 2D EBSD IPF-z map of 5 nearest neighbor grains (1-2-3-4-5) with multiple twin orientation relationships and the attached TiC particle in purple, taken from an EBSD slice in the 3D equiaxed zone. Twin grain boundaries are shown in white and regular grain boundaries are shown in black. (b) Corresponding colored pole figure $\langle 110 \rangle$ of grains from 1 to 5 that share a common $\langle 110 \rangle$ direction, highlighted in a red pentagon shape. The $\langle 110 \rangle$ directions of the TiC particle are represented by purple stars that have no common orientation relationship with the FCC grains.

of a few nanometers [32]. These imaging conditions allow to observe a particle in the center of the TiC (probably an oxide as in Figure 5(b)), several equiaxed grains of fcc-Ni, recognizable by the different light gray contrasts, but also numerous precipitates whose size does not exceed a hundred nanometers. These precipitates were not visible at 15 and 10 kV, indicating that their thickness in the volume is also $< 100\,\mathrm{nm}$. Some of these precipitates nucleate and grow directly on the TiC particle, while others are not in direct contact with the particle. This can also be observed in Figure 7(b), where numerous precipitates with different gray contrasts, labeled A (dark gray) and B (light gray), can be seen in the eutectic region a few microns away from a TiC particle. Due to their size and fraction, the nanoprecipitates could not be identified by EBSD or XRD. Therefore, transmission electron microscopy was used and the analysis is presented in the next section.

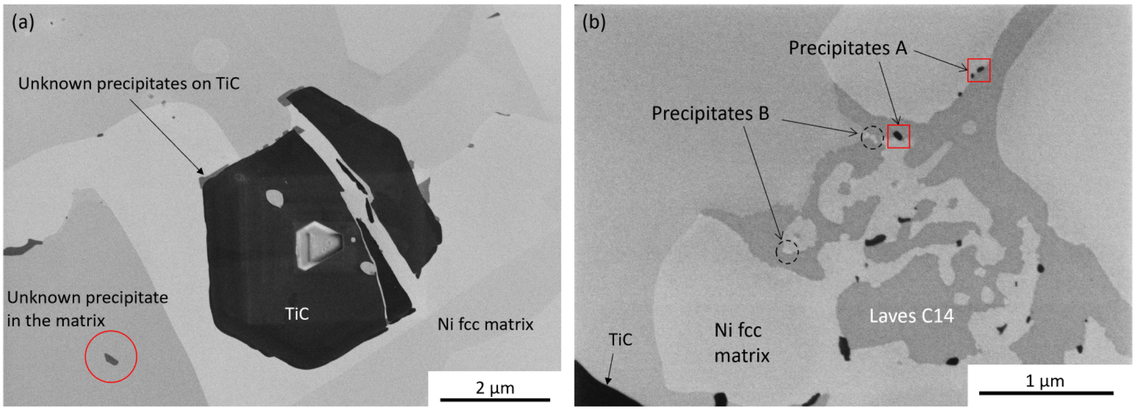

Figure 7: SE image using the InLens detector at 1 kV of (a) a TiC particle in the equiaxed grain region. Various unknown precipitates grow on the surface of the cracked TiC. Some other undetermined nano-sized precipitates can also be seen in the matrix a few microns around the TiC particle; (b) unknown precipitates of different contrasts, labeled A (dark) and B (lighter gray), in the eutectic region between the Laves phase C14 and the matrix FCC in the equiaxed grain zone.

3.2. Transmission Electron Microscopy analysis of nano-precipitates

As shown in the previous paragraph, TiC particles appear to play an important role in the formation of the equiaxed zone in Inconel 718 produced by the laser wire AM process. However, TiC particles are found in both the columnar and equiaxed zones in the samples that were characterized. It should be recalled that the position of the equiaxed zone was found to be unusual: it is close to the interface with the previous layer, while the upper part of the layer is completely columnar (see supplementary information in [9]). To better understand this phenomenon, thin foils containing a carbide particle were taken from the columnar zone and from the equiaxed zone for comparison.

Figure 8 shows a bright field TEM image and EDS maps of the TiC particles in the columnar zone (Figure 8(a)) and in the equiaxed zone (Figure 8(b)). The elements included in the EDS analysis are indicated on the maps. On each map the TiC particle is indicated and can be easily identified by the Ti EDS map. Striking differences can be observed between the TiC of the columnar and equiaxed zones. First, their morphology is very different: in the columnar zone TiC have a rounded shape while in the equiaxed zone it is faceted. The presence of matrix elements can be seen inside the particle taken from the columnar zone, whereas the particle from the equiaxed region contains only the (Mg,Al) oxide on which it has probably nucleated. These two observations suggest that the TiC particle in the columnar zone is melting and/or dissolving as it grows in the equiaxed zone. Then, considering the chemical environment of the particle, Figure 8(a-b) also show some differences. In Figure 8(a), the TiC particle is covered with Nb and C to a lesser extent. Diffraction studies of this region (not shown here) have shown that it corresponds to niobium carbide NbC growing epitaxially from the TiC. In Figure 8(b) the microstructure is more complex. Again, some NbC is observed on some facets of the TiC but does not cover the entire particle.

A single NbC particle is also observed in the upper right part of the images. A local enrichment of Mg at the surface of the TiC particle is visible in the figure. It corresponds to an fcc $Mg_{0.32}Ti_{0.68}$ precipitate (space group Fm-3m, cF4 $a = 0.442\,\mathrm{nm}$ [33]) with the same orientation as the TiC. Finally, in the center left of Figure 8(b), an Nb-enriched zone can be observed that is not enriched in carbon. This region, in which the Nb content is about $30\,\mathrm{wt\%}$, will be further investigated in the following.

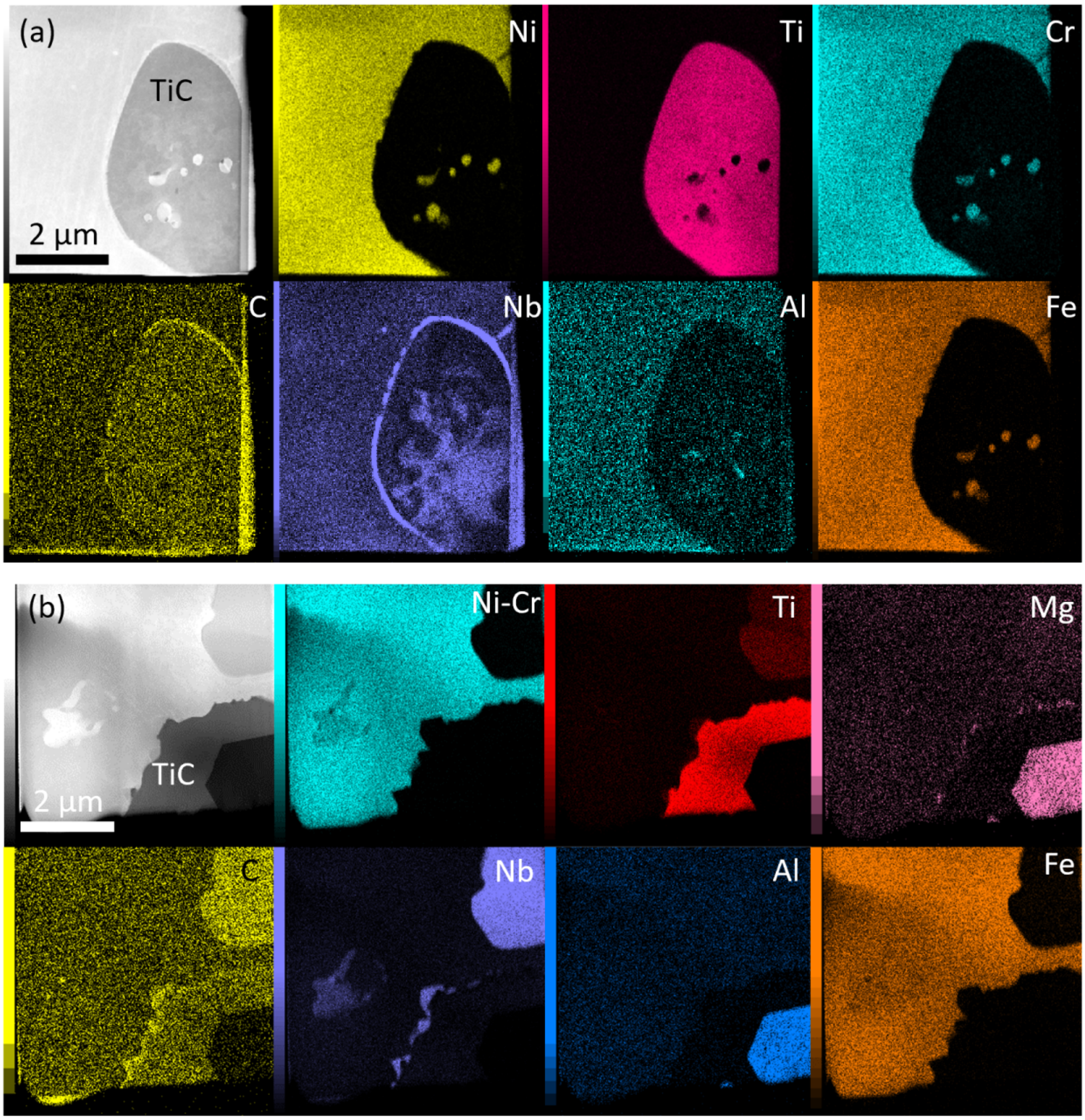

Figure 8: HAADF STEM image and EDS maps of element distribution around: (a) a TiC particle in the columnar grain zone and (b) a TiC particle in the equiaxed zone.

A zoom in on the interface between the TiC and the fcc matrix in the equiaxed zone is shown in Figure 9(a). On the right part of the TiC, the EDS map shows a NbC with Mg segregation between the TiC and the NbC. On the left side of the image, a precipitate enriched in Nb without any C can be observed (circle in Figure 9(a)). This precipitate is shown in the TEM bright field micrograph in Figure 9(b). It is identified as the Nb_2Ni phase, which is a cubic C15 Laves phase (space group Fd-3m, Pearson symbol cF96) with $a = 1.183\,\mathrm{nm}$ measured from the diffraction pattern in Figure 8(c). This phase was recently discovered by Zhao *et al.* [34] in an Nb-Ni binary alloy with a similar measured lattice parameter of $a = 1.188\,\mathrm{nm}$. It is unexpected that this phase forms in Inconel 718, which contains only $5\,\mathrm{wt\%}$ Nb. It means that the local Nb enrichment observed around the TiC particle leads to the formation of metastable phases such as Nb_2Ni. This Nb_2Ni precipitate has no obvious orientation relationship with the TiC or the fcc matrix.

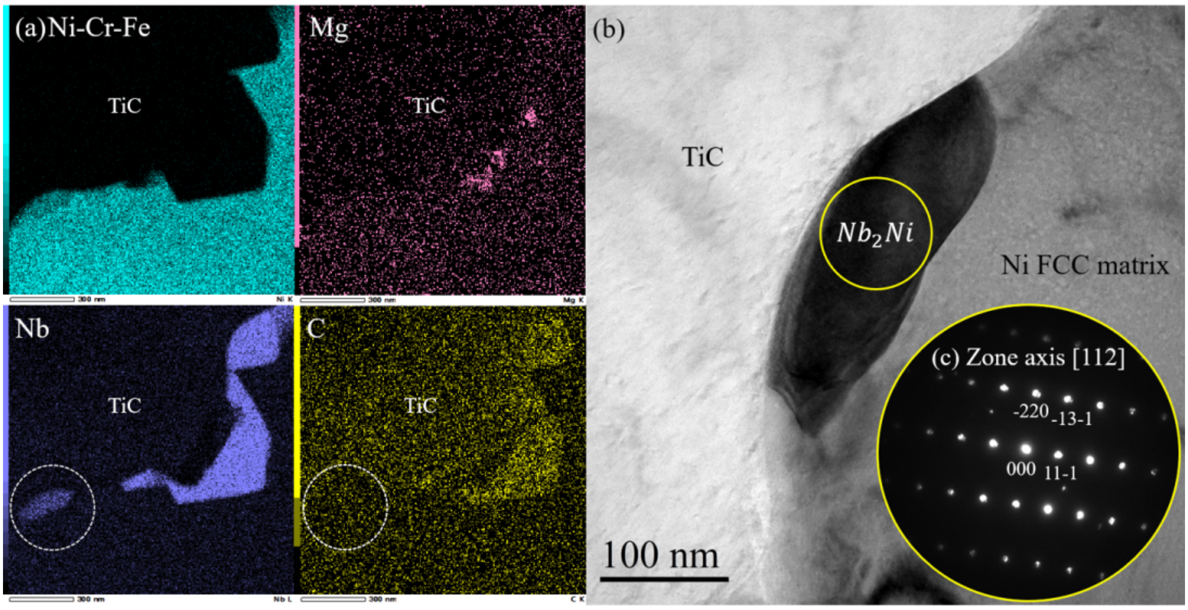

Figure 9: (a) EDS map of the interface between the TiC and the FCC matrix in the equiaxed grain zone showing the presence of Mg segregation within the NbC phase. A circled precipitate enriched in Nb is analyzed in TEM (b) BF-TEM micrograph of the Nb enriched precipitate identified as the Laves phase Nb_2Ni with electron diffraction pattern (c) along the [112] zone axis.

Figure 10(a) shows a STEM image of the same zone previously analyzed in Figure 8. The TiC particle, the matrix and the previously observed Nb enriched zone (Figure 8(b)) can be seen in Figure 10(a) with different areas of interest labeled from 1 to 3. In region 1, the electron diffraction pattern of the Nb-rich layer on the TiC particle confirms that it is a NbC whose diffraction pattern along the $[110]$ zone axis is shown in Figure 10(b). The lattice parameter of NbC (space group Fm-3m, Pearson symbol cF8 and $a = 0.4691\,\mathrm{nm}$ [35]) was found to be $a = 0.435\,\mathrm{nm}$ which is lower than the literature values. Area 2 corresponds to a locally Nb-enriched matrix, a high resolution TEM (HRTEM) image of area 2 is shown in Figure 10(c). At the bottom of this image, the Fast Fourier Transform (FFT) of the region marked by the red square in this micrograph shows that the matrix is oriented along the $[100]$ zone axis. The FFT corresponding to the red rectangle at the top of figure 10(c) (in the Nb-rich zone) shows a local difference within the matrix. In this region, in addition to the matrix diffraction spots, the ring shows a slightly amorphous structure as well as other diffracted spots that could not be indexed. Some spots are shared with the matrix in the FFT, indicating that there is an orientation relationship between the two phases. Due to the size of this area ($\approx .5\,\mathrm{nm}$), this could be the result of an overlap between phases in the thin foil. Area 3 corresponds to the large Nb-rich zone in Figure 8 and is shown in Figure 10(d).

At the scale of the HRTEM image, the FFTs taken from two zones of the image again indicate that the region contains multiple phases. The first FFT (at the top of the image) shows a structure similar to a theoretical 2-fold symmetry axis of an iQC [36]. However, due to the size of this region, which contains only a few hundred atoms, it was not possible to rotate and tilt the thin foil further to identify the corresponding 3- and 5-fold symmetry axes to confirm an icosahedral order. The FFT at the bottom of the image in Figure 9(d) shows a diffracted ring, again indicating a slightly amorphous structure, as well as a structure that could not be determined. The complex microstructure on the scale of a few tens of nanometers in this Nb-rich region shows the need for further characterization.

This was done using automated crystal orientation maps (ACOM). In addition to the "equilibrium" phases, *i.e.* the γ-fcc matrix, the Laves phase C14 Ni_2Nb, and the niobium carbide NbC, other Nb-rich phases were considered: Nb_2Ni (which was observed in Figure 9), Ni_6Nb_7 (space group R-3m, Pearson symbol hR39, $a = 0.4893\,\mathrm{nm}$ and $c = 2.6640\,\mathrm{nm}$ [37]) and Nb_5Ni (space group Fd-3m, $a = 1.1642\,\mathrm{nm}$ [38]). Figs. 11(a)-b show the result of ACOM of the area labeled 3 in Figure 10 with the correlation index map and the indexed phase map, respectively. The correlation index map in Figure 11(a) shows a large dark zone where no phases could be indexed. The different acquired diffraction patterns of the phases identified in Figure 11(b) with the simulated ones are shown in Figure 11(c). The phase reliability parameter, denoted R, is given for each phase. If this parameter is greater than 15, it is considered that the ACOM analysis is accurate enough to identify the phase [27]. The fcc matrix is perfectly indexed as shown in Figure 11(c) with a R value of 45. The NbC was also indexed with a very high R index. The TiC was indexed with a lower R value. Besides the diffraction ring generated by an amorphous phase, some spots could not be indexed. A small area was indexed as Laves phase Ni_2Nb with $R = 7$, which is not sufficient to say that there is Laves phase C14 in this area. The phase Ni_6Nb_7 is indexed with $R = 18$, which is lower than the matrix and the NbC phases.

The Ni_6Nb_7 phase shows unindexed and missing spots. This is probably due to the small thickness of the precipitate, which overlaps with other phases within the thin foil thickness. The unindexed areas (dark areas in Figure 11(a)) indicate that some phases are missing, which should be taken into account for the ACOM analysis. Most of the known phases for this system have been entered, which means that these missing phases may still be discovered. Nevertheless, the identification of Ni_6Nb_7, Nb_2Ni, $Mg_{0.32}Ti_{0.68}$ and the observation of several unknown phases shows the complexity of phase formation around TiC particles in the non-equilibrium solidification conditions associated with the LMD-W process.

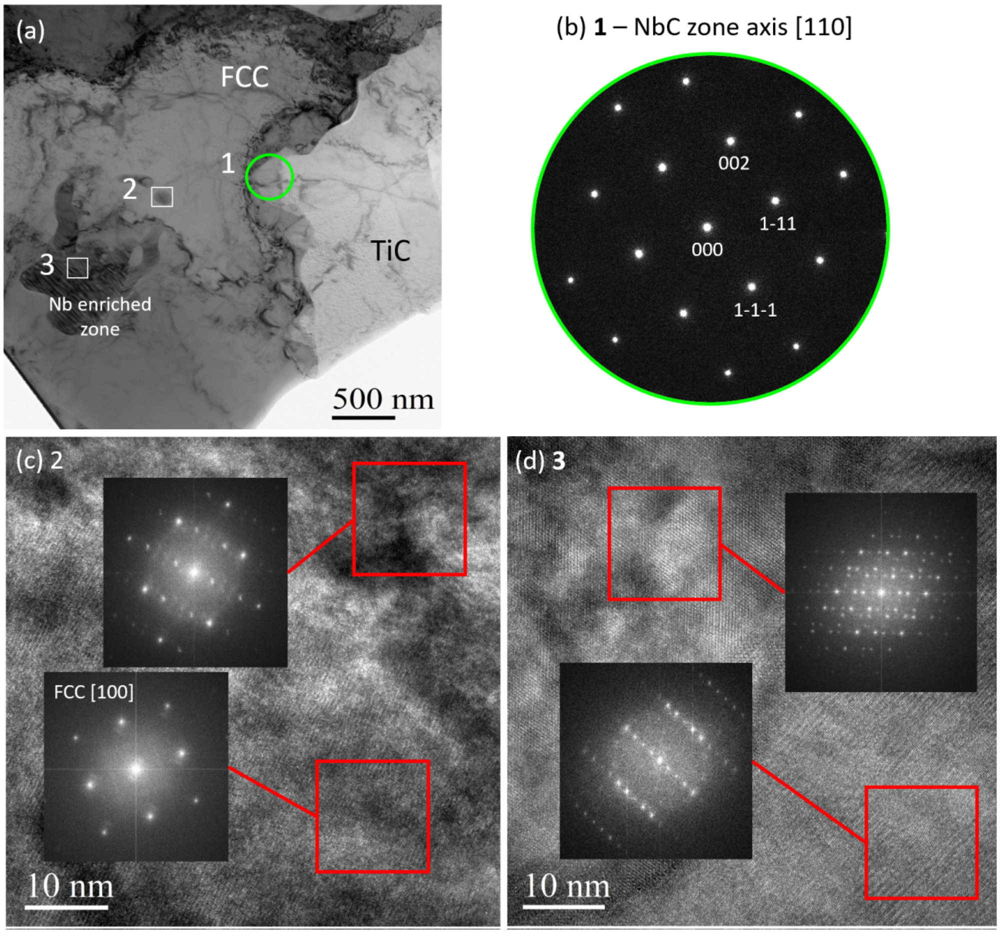

Figure 10: (a) BF-TEM micrograph of the TiC particle, the matrix fcc and the Nb enriched zone, with analyzed local areas labeled 1 to 3. (b) Electron diffraction pattern of the zone axis [110] of the NbC in the area labeled 1. (c) High resolution transmission electron micrograph (HRTEM) of region 2 with Fast Fourier Transform (FFT) of two different grains, one of which is identified as matrix fcc (d) HRTEM micrograph and FFT images of two grains with unknown structures in region 3.

4. Discussion

The aim of this study is to investigate the origin of the ISRO-induced nucleation mechanism observed by the authors for the first time in a nickel alloy [9]. The coupled EDS-EBSD 3D analysis showed that the multi-twinned grain boundaries originate close to the titanium carbides. Further investigation by TEM showed that a large number of phases nucleated on and around these carbides. Do these phases serve as heterogeneous nucleation sites for the fcc structure of nickel, producing multi-twinned grains? A first interesting observation is that among the Nb-rich phases identified, all of them contain icosahedral clusters in their lattice structure, as shown in Figure 12. In this figure, the crystal structure of Ni_6Nb_7, Nb_2Ni and Ni_2Nb is shown, with the Ni atoms in blue color and the Nb atoms in orange color. For each structure, the icosahedral cluster types are shown with different colors according to their orientation in the lattice. The labels A to E indicate different cluster types depending on their atomic environment and their

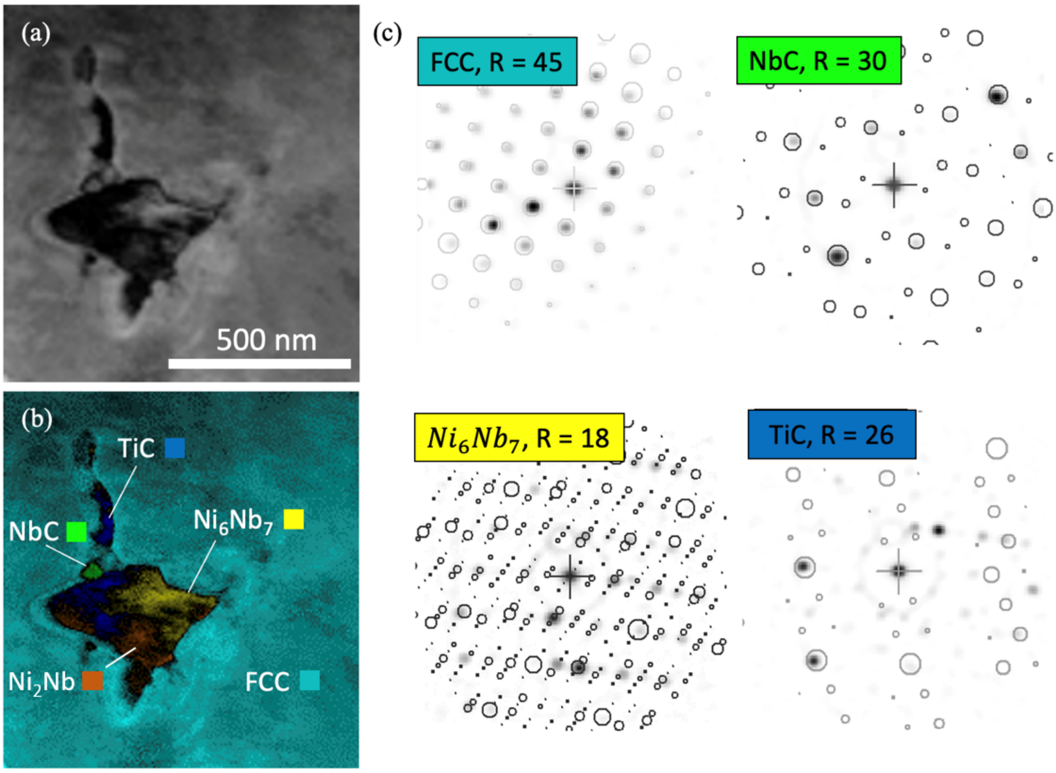

Figure 11: (a) ACOM correlation index map of the Nb enriched region in the equiaxed grain zone (b) phase + correlation index map (c) acquired diffraction patterns of the different phases compared to the simulated patterns.

distortion with respect to an ideal icosahedron. Ni_6Nb_7 contains two different types of icosahedral clusters, labeled A and B in Figure 12(a), each with a single orientation in the lattice. Nb_2Ni have only one type of icosahedral cluster, which differs only in its orientation in the lattice, as shown in Figure 12(b). Finally, the Ni_2Nb structure (Figure 12(c)) contains two types of icosahedral clusters labeled D and E, where D has two possible orientations.

For all these icosahedral cluster types, and to further investigate the possible relationship between the Nb-rich phases and the fcc-Ni matrix, additional aspects of the crystal structure were analyzed. Since the orientation relationship between the icosahedron and the fcc phase is $\langle 110 \rangle_{\mathrm{fcc}} \parallel$ 5-fold axis [12], the directions of the 5-fold axes were determined for all clusters and correspond to the direction between the atom in the center and the vertices of the icosahedron. These directions are given in Table 2.

In order to serve as a possible heterogeneous nucleation site for the fcc-Ni phase, a nucleant particle should have a good atomic match with the phase it is to serve as a catalyst. Again considering the ISRO-mediated nucleation mechanism, the atomic mismatch between the icosahedron cluster facets and the $\{111\}$ plane of fcc-Ni was determined using the Bramfitt atomic mismatch criterion [39]. The range of atomic mismatch, in percent, is also given in Table 2. Bramfitt showed that heterogeneous nucleation and growth is effective below $6\,\%$ of mismatch, moderately effective for 6 to $12\,\%$, and least effective above $12\,\%$. From the table it can be seen that while some facets have relatively low atomic mismatch with the fcc-Ni matrix, most of them have values greater than $10\,\%$.

Finally, the directions of the 5-fold axes were compared with the $\langle 110 \rangle$ direction of the surrounding fcc-Ni grains using the grain orientation data and to establish possible orientation relationships. No correlation could be found between fcc-Ni and the Nb-rich phases, nor with the 5-fold axis contained in the crystal structure. This implies that the fcc-Ni phase nucleated by the ISRO-mediated mechanism and the various Nb-rich phases containing icosahedral clusters nucleated and grew independently.

A remaining question is how such niobium-rich phases can form in Inconel 718, which contains only 5%Nb. Since Ni_6Nb_7, Nb_2Ni and Ni_2Nb were observed only in the vicinity of the titanium carbide particles, TiC seems to play a key role in their formation. In the columnar zone (Figure 8(a)), where the TiC particles appear to dissolve, they are capped with niobium carbide, which means that NbC is more stable. The presence of TiC even seems to stabilize NbC in pure nickel [40]. The dissolution of TiC releases C in the Nb-containing liquid and NbC can grow epitaxially on the TiC. In the equiaxed zone, the TiC particles appear more stable and there is no C enrichment of the liquid phase around these particles. However, if there is a driving force to form NbC – and there is, because NbC were also observed in the equiaxed zone (Figure 8(b)) and there is no carbon available in the liquid, Nb could simply accumulate around the TiC particles, as the reaction rate to form NbC would be much slower in this case. This could explain the local enrichment of Nb around the TiC particle and partially explain the formation of Nb-rich phases. Figure 13 shows

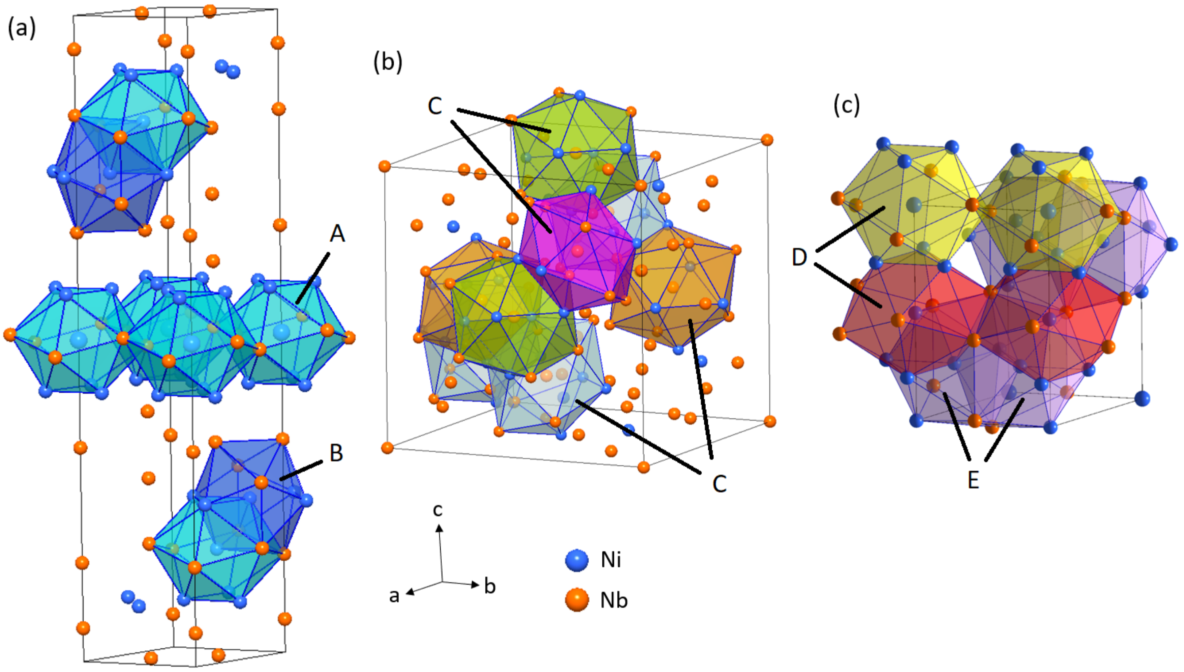

Figure 12: Crystal structure of (a) Ni_6Nb_7 (b) Nb_2Ni (c) C14 Ni_2Nb, where Ni atoms are blue and Nb atoms are orange. Distorted icosahedra in the structures (corresponding to Frank-Kasper polyhedra with a coordination number of 12) are represented by a color corresponding to their orientation type: A and B for Ni_6Nb_7, C for Nb_2Ni, D and E for Ni_2Nb.

Phase	Icosahedron type	Direction family $\langle uvw \rangle$ of 5-fold symmetry axes	Atomic mismatch % (min-max) with fcc
Ni_6Nb_7	A	$\langle 4\,0\,3 \rangle$ $\langle 4\,4\,3 \rangle$ $\langle 1\,0\,9 \rangle$ $\langle 1\,1\,9 \rangle$	0.01 – 24.59
	B	$\langle 2\,2\,9 \rangle$ $\langle 7\,7\,53 \rangle$ $\langle 3\,3\,32 \rangle$ $\langle 1\,2\,0 \rangle$ $\langle 17\,17\,181 \rangle$ $\langle 1\,1\,9 \rangle$ $\langle 51\,51\,539 \rangle$	10.38 – 29.92
Nb_2Ni	C	$\langle 4\,4\,23 \rangle$ $\langle 41\,61\,41 \rangle$	12.13 – 56.70
Ni_2Nb	D	$\langle 0\,5\,13 \rangle$ $\langle 5\,5\,13 \rangle$ $\langle 95\,0\,32 \rangle$ $\langle 0\,4\,1 \rangle$ $\langle 95\,95\,32 \rangle$ $\langle 181\,0\,61 \rangle$ $\langle 181\,181\,61 \rangle$	3.53 – 89.02
	E	$\langle 1\,2\,0 \rangle$ $\langle 2\,2\,4 \rangle$ $\langle 5\,5\,13 \rangle$ $\langle 0\,5\,13 \rangle$ $\langle 18\,18\,61 \rangle$	16.55 – 51.69

Table 2: Lattice mismatch variation per icosahedron of the different Nb enriched phases with the fcc system.

an isopleth section of Inconel 718 with varying Nb content in the temperature range relevant to the solidification of the alloy, *i.e.* between the liquidus and solidus temperatures for the nominal composition range of the alloy (about $5\,\mathrm{wt\%}$ Nb). The different curves in Figure 13 show the values below which there is a thermodynamic driving force for the different phases. As expected, the C14 Laves phase Ni_2Nb can form when the Nb content reaches 16 - 21 $\%$, which is naturally observed in the interdendritic regions due to microsegregation. It is worth noting that the Nb_2Ni phase is able to form when the Nb content reaches 55 - 60 %, which proves the important local Nb enrichment in the periphery of the TiC. The Ni_6Nb_7 phase is stable at lower, but still quite high Nb contents of about 38 to 42 %. All of these phases form in the solidification temperature range, which means they formed from the liquid phase. In Figure 13 the composition that can lead to amorphous structure is also indicated (literature values for binary Ni-Nb alloys [41, 42]). From 37.5 wt% Nb, Lu *et al.* [41] show the presence of amorphous structure for $Ni_{62.5}Nb_{37.5}$ among the glassy Ni-Nb alloys. They also emphasized the presence of ISRO. ISRO is present in amorphous structures for a wide range of Nb compositions and temperatures [42]. This is also consistent with some TEM observations of locally slightly amorphous regions (Figure 9).

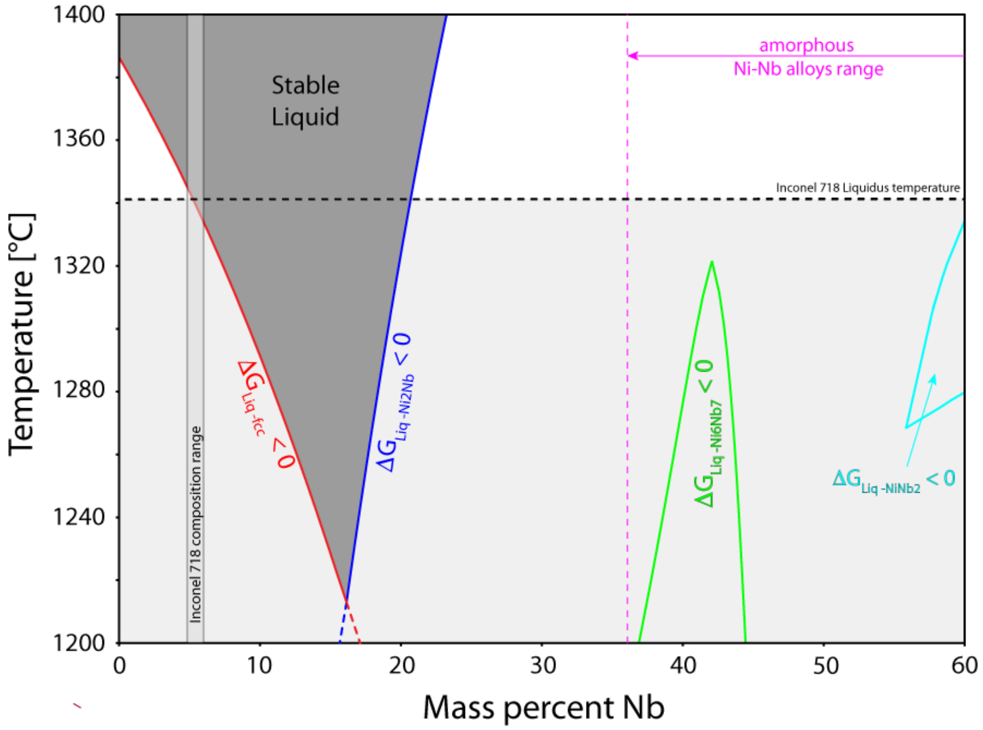

Figure 13: Isopleth section of Inconel 718 - Nb system in the solidification temperature range. The nominal composition range of Inconel 718 is given for 5 wt% Nb. The boundaries between the driving forces ΔG of the solid phase formation and the liquid are represented by different colors for each phase. The field under which the fcc phase forms is highlighted by the red curve. The formation of the Laves phase C14 Ni_2Nb is highlighted in blue. The Ni_6Nb_7 phase forms from 37 to 44 % Nb and is shown in green, while for higher Nb contents (55-60 %) the Nb_2Ni phase appears.

In summary, it is demonstrated that the favorable temperature conditions induced by the LMD-W process in the region where equiaxed grains are observed lead to local Nb enrichment around the TiC particles. 3D coupled EDS-EBSD analysis revealed that ISRO-mediated nucleation of the fcc-Ni occurs in the vicinity of the TiC particles, and TEM observations revealed that many phases containing icosahedral clusters, namely Ni_6Nb_7, Nb_2Ni and Ni_2Nb, also

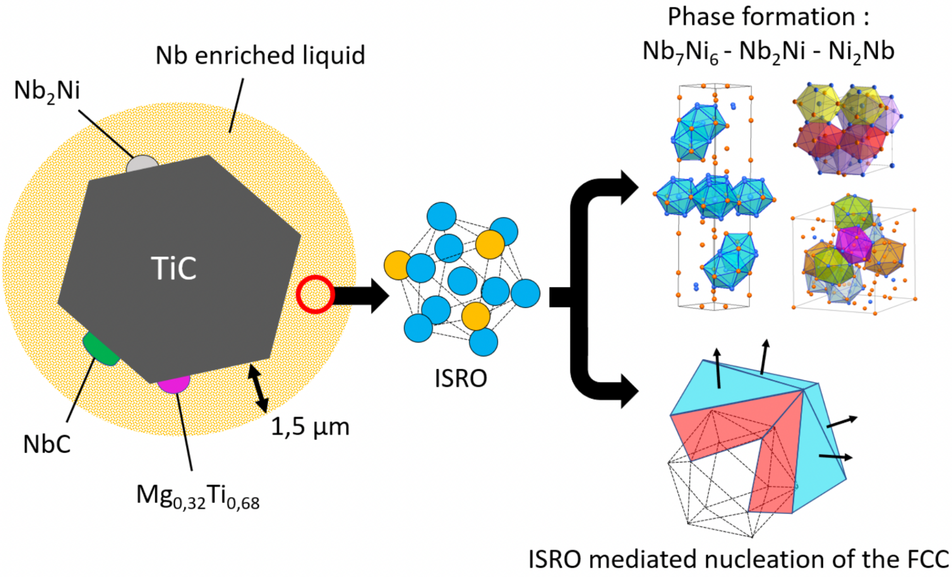

Figure 14: Schematic representation of the enriched Nb liquid surrounding the TiC particles, which promotes different phase formations. ISRO is promoted by Nb enrichment, which can induce the characterized Ni_6Nb_7 and Nb_2Ni phases, as well as ISRO-mediated nucleation of the fcc phase.

nucleate around the TiC particle. All of these phases occur in the same temperature range and have no orientation relationship, indicating that they all form simultaneously. These results are shown in Figure 14. TiC leads to local enrichment of Nb in the liquid. Such Nb-rich zones favor ISRO in the liquid, leading to ISRO-mediated nucleation of the fcc-Ni phase and nucleation of various phases independently of the fcc-Ni phase, some of which contain a high density of icosahedral clusters and are unprecedented in Inconel 718. Such a scenario explains why 5-fold symmetry axes are observed in the vicinity of TiC and appear to emerge from it on 3D characterization.

5. Conclusion

In this work, the equiaxed region of Inconel 718 processed by the LMD-W process was characterized by 3D coupled EDS-EBSD analysis and HRTEM. The conclusions of this study are as follows.

- 3D characterization of the equiaxed grain zone using both EBSD and EDS revealed a fraction of grains with a twinning orientation relationship of $12.2\,\%$ and a volume fraction of TiC particles of $1\,\%$. The identification of a 5-fold symmetry axis, corresponding to a $\langle 110 \rangle$ direction common to 5 fcc grains, was found to originate from a TiC particle.
- High resolution imaging in SEM and TEM revealed many nanometer sized precipitates around the TiC particles. The structure of most of them, especially the smallest ones ($\leq 5\,\mathrm{nm}$), remains unresolved. In addition to the commonly observed C14 Laves phase, this work reports the first observation of Ni_6Nb_7 and Nb_2Ni in Inconel 718.

- The comparison of TiC particles in the columnar and equiaxed zones revealed a local enrichment of Nb in the particle environment. In the columnar zone, located in higher temperature regions, the TiC dissolves and leads to the formation of a NbC shell around the TiC. In the equiaxed region, which is closer to the melt pool boundaries and experiences temperatures close to the liquidus temperature of the alloy, the TiC remains stable.
- The local Nb enrichment in the liquid around the TiC particles is thought to promote ISRO in the liquid, leading to the formation of Nb-rich phases containing icosahedral clusters and to the ISRO-mediated nucleation mechanism of the fcc-Ni phase.

Acknowledgements

This work was funded by the INTERREG VA ”Grande Region” program ”FAFIL” No. 050-4-08-126, and by ANRT France under a CIFRE Ph.D. scholarship (grant number 2018-1630). The authors thank S. Migot for the extraction of the thin films and M. Emo for the help with the ASTAR software.

References

[1] B. T. Gibson, Y. K. Bandari, B. S. Richardson, W. C. Henry, E. J. Vetland, T. W. Sundermann, L. J. Love, Addit. Manuf. 32 (2020) 100993.
[2] A. Baghdadchi, V. A. Hosseini, M. A. V. Bermejo, B. Axelsson, E. Harati, M. Högström, L. Karlsson, Materials 14 (2021) 7170.
[3] T. Bergs, S. Kammann, G. Fraga, J. Riepe, K. Arntz, Procedia CIRP 94 (2020) 29–34.
[4] M. Akbari, R. Kovacevic, Addit. Manuf. 23 (2018) 487–497.
[5] Y. Tian, N. Chekir, X. Wang, A. Nommeots-Nomm, R. Gauvin, M. Brochu, Addit. Manuf. 24 (2018) 137–144.
[6] M. He, H. Cao, Q. Liu, J. Yi, Y. Ni, S. Wang, Addit. Manuf. 55 (2022) 102839.
[7] G. Sujan, H. Li, Z. Pan, D. Liang, N. Alam, Addit. Manuf. 51 (2022) 102602.
[8] M. Bambach, I. Sizova, F. Kies, C. Haase, Addit. Manuf. 47 (2021) 102269.
[9] I. Cazic, J. Zollinger, S. Mathieu, M. El Kandaoui, P. Plapper, B. Appolaire, Scripta Mater. 195 (2021) 113740.
[10] I. Cazic, Coaxial laser wire additive manufacturing of Inconel 718, Ph.D. thesis, Université de Lorraine, 2022.
[11] G. Kurtuldu, P. Jarry, M. Rappaz, Acta Mater. 61 (2013) 7098–7108.
[12] G. Kurtuldu, A. Sicco, M. Rappaz, Acta Mater. 70 (2014) 240–248.
[13] C. Galera-Rueda, X. Jin, J. LLorca, M. Pérez-Prado, Scripta Mater. 211 (2022) 114512.
[14] P. Liu, Z. Wang, Y. Xiao, M. F. Horstemeyer, X. Cui, L. Chen, Addit. Manuf. 26 (2019) 22–29.
[15] N. Raghavan, B. C. Stump, P. Fernandez-Zelaia, M. M. Kirka, S. Simunovic, Addit. Manuf. 47 (2021) 102209.
[16] S. Li, J. Li, Z. Jiang, Y. Cheng, Y. Li, S. Tang, J. Leng, H. Chen, Y. Zou, Y. Zhao, et al., Addit. Manuf. (2022) 102958.
[17] R. Krakow, D. N. Johnstone, A. S. Eggeman, D. Hünert, M. C. Hardy, C. M. Rae, P. A. Midgley, Acta Mater. 130 (2017) 271–280.
[18] J. Häglund, A. F. Guillermet, G. Grimvall, M. Körling, Phys. Rev. B 48 (1993) 11685.
[19] A. Segerstark, J. Andersson, L.-E. Svensson, O. Ojo, Mater. Charact. 142 (2018) 550–559.
[20] A. Pautrat, Étude expérimentale quantitative de la solidification de l'inconel 718 en fonderie, Ph.D. thesis, Paris, ENMP, 2013.
[21] Y. Zhao, K. Li, M. Gargani, W. Xiong, Addit. Manuf. 36 (2020) 101404.
[22] V. V. Rielli, A. Piglione, M.-S. Pham, S. Primig, Addit. Manuf. 50 (2022) 102540.
[23] J. Zollinger, B. Rouat, J. Guyon, S. Pillai, M. Rappaz, Metall. Mater. Trans. A 50 (2019) 2279–2288.
[24] M. Buttard, G. Martin, X. Bataillon, G. Renou, P. Lhuissier, J. Vilanova, B. Chehab, P. Jarry, J.-J. Blandin, P. Donnadieu, Additive Manufacturing (2022) 103313.

[25] D. N. Johnstone, B. H. Martineau, P. Crout, P. A. Midgley, A. S. Eggeman, J. Appl. Crystallogr. 53 (2020) 1293–1298.

[26] E. Rauch, M. Véron, Mater. Charact. 98 (2014) 1–9.

[27] A. Després, C. Mayer, M. Véron, E. Rauch, M. Bugnet, J.-J. Blandin, G. Renou, C. Tassin, P. Donnadieu, G. Martin, Materialia 15 (2021) 101037.

[28] J.-O. Andersson, T. Helander, L. Höglund, P. Shi, B. Sundman, Calphad 26 (2002) 273–312.

[29] J. Mackenzie, Biometrika 45 (1958) 229–240.

[30] K. Aigner, W. Lengauer, D. Rafaja, P. Ettmayer, Journal of alloys and compounds 215 (1994) 121–126.

[31] M. Rappaz, P. Jarry, G. Kurtuldu, J. Zollinger, Metall. Mater. Trans. A 51 (2020) 2651–2664.

[32] D. C. Bell, N. Erdman, Low voltage electron microscopy: principles and applications, John Wiley & Sons, 2012.

[33] S. Rousselot, M.-P. Bichat, D. Guay, L. Roué, Journal of the Electrochemical Society 156 (2009) A967.

[34] J. Zhao, H. Wang, B. Wei, J. Mater. Sci. Technol. 100 (2022) 246–253.

[35] R. Wyckoff, Crystal structures 1 (1963) 85–237.

[36] F. Fang, J. Kovacs, G. Sadler, K. Irwin, arXiv preprint arXiv:1311.3994 (2013).

[37] X. Liu, X. Zhang, H. Jiang, S. Yang, Z. Shi, C. Wang, Int. J. Mater. Res. 108 (2017) 767–775.

[38] P. Kripyakevich, E. Pylaeva, Sov. Phys. Crystallogr. 12 (1967) 294–296.

[39] B. L. Bramfitt, Metall. Trans. 1 (1970) 1987–1995.

[40] L. da Costa Morais, F. Beneduce, R. Magnabosco, A. L. N. da Silva, Int. J. Refract. Hard Met. 105 (2022) 105826.

[41] W. Lu, J.-C. Tseng, A. Feng, J. Shen, J. Non-Cryst. 564 (2021) 120834.

[42] T. Wen, Y. Zhang, C.-Z. Wang, N. Wang, K.-M. Ho, M. J. Kramer, Intermetallics 98 (2018) 131–138.